Combining Acoustic Trapping With Plane Wave Imaging for Localized Microbubble Accumulation in Large Vessels

Luzhen Nie, *Student Member, IEEE*, Sevan Harput, David M. J. Cowell, Thomas M. Carpenter, James R. McLaughlan, and Steven Freear, *Senior Member, IEEE*

Abstract—The capability of accumulating microbubbles using ultrasound could be beneficial for enhancing targeted drug delivery. When microbubbles are used to deliver a therapeutic payload, there is a need to track them, for a localized release of the payload. In this paper, a method for localizing microbubble accumulation with fast image guidance is presented. A linear array transducer performed trapping of microbubble populations interleaved with plane wave imaging, through the use of a composite pulse sequence. The acoustic trap in the pressure field was created parallel with the direction of flow in a model of a vessel section. The acoustic trapping force resultant from the large gradients in the acoustic field was engendered to directly oppose the flowing microbubbles. This was demonstrated numerically with field simulations, and experimentally using an Ultrasound Array Research Platform II. SonoVue microbubbles at clinically relevant concentrations were pumped through a tissue-mimicking flow phantom and exposed to either the acoustic trap or a control ultrasonic field composed of a single-peak acoustic radiation force beam. Under the flow condition at a shear rate of 433 s^{-1}, the use of the acoustic trap led to lower speed estimations ($p < 0.05$) in the center of the acoustic field, and an enhancement of $71\% \pm 28\%$ ($p < 0.05$) in microbubble image brightness.

Index Terms—Acoustic radiation force (ARF), acoustic trap, atherosclerosis, diagnostic ultrasound, microbubbles, plane wave imaging (PWI), sonothrombolysis, targeted drug delivery, ultrasound contrast agents.

I. INTRODUCTION

THE widespread employment of microbubbles as ultrasound contrast agents is attributed to their strong scattering capabilities and relative safety. The clinical use of microbubbles is to enhance the contrast in echocardiography [1] and improve the visualization of liver perfusion [2], and so on. It is suggested that asymmetric microbubble oscillations across ultrasonic compression and rarefaction phases are responsible for the generation of harmonics [3], in addition to scattering of higher harmonics due to nonlinear propagation [4]. Contrast imaging modalities which investigate microbubble nonlinear fundamental and second harmonic oscillations have been implemented in the commercial systems [5]. Myriad techniques that use microbubble subharmonic [6] and superharmonic [7] frequencies are being explored to further improve the image quality. In recent years, high frame-rate ultrasound, which typically uses nonfocused plane/diverging wave transmissions [8], [9], has been combined with microbubbles [10]–[12], which has led to nondestructive microbubble detection at frame rates two orders of magnitude higher than the established line-by-line imaging mode. The large amount of data in high frame-rate contrast-enhanced ultrasound has created a renewed interest in simultaneous Doppler and perfusion imaging [13] and provided opportunities for super-resolution imaging [14].

The therapeutic use of microbubbles is currently an area of great interest. Microbubble volumetric vibrations can be actively driven by the use of ultrasound [15], and the associated biomechanical effects have been used as a mechanism to break up blood clots since the 1990s [16]. For sonoporation, the enhanced cell membrane permeability caused by localized microbubble oscillations [17], has been shown to improve uptake of coadministered therapeutics [18], [19]. Microbubbles can also be engineered as drug vehicles and payload release can be activated through the external acoustic fields at specific locations [20], [21]. Following intravenous injections, a low microbubble concentration in the region of interest (ROI) can hamper their therapeutic potential for sonothrombolysis [22] or trans-membrane drug delivery [23]. Conjugating microbubbles with antibodies, can target them to vascular receptors with high specificity [24], but some approaches can elicit an immune system response [25]. Furthermore, the targeting efficiency is reduced in the presence of high flow rates [26]. Microbubbles preferentially travel along the centerline of a vessel where the flow is fastest, which reduces binding further in large vessels, as they are not in the proximity of the diseased blood vessel endothelium. To address these

L. Nie, D. M. J. Cowell, T. M. Carpenter, and S. Freear are with the Ultrasonics and Instrumentation Group, School of Electronic and Electrical Engineering, University of Leeds, Leeds LS2 9JT, U.K. (e-mail: elln@leeds.ac.uk; s.freear@leeds.ac.uk).

S. Harput is with the Department of Bioengineering, Imperial College London, London SW7 2BP, U.K.

J. R. McLaughlan is with the Ultrasonics and Instrumentation Group, School of Electronic and Electrical Engineering, University of Leeds, Leeds LS2 9JT, U.K., and also with the School of Medicine, Leeds Institute of Cancer and Pathology, University of Leeds, Leeds LS9 7TF, U.K.

limitations, acoustic radiation force (ARF) has been used to manipulate the position of microbubbles to the distal vascular wall in order to facilitate the cellular binding [27]–[30] and locally increase the microbubble concentration.

An alternative approach to ARF is the use of magnetic nanoparticle-doped microbubbles that can be manipulated by an external magnetic field [31]. *In vitro* [32] and *in vivo* [33] studies demonstrated that magnetic targeting of microbubbles can be achieved with a constrained depth of 20 mm. The use of optimized magnetic arrays could achieve improved targeting performance in terms of depth and accuracy [34]. These optimized arrays are comprised of multilayer permanent magnet elements, generating the maximum field strength at a position of interest. Unfortunately, implementing this technique is difficult, since optimizations are valid only for specific depths.

Locally accumulating microbubbles over time would promote interactions with the diseased tissue in space, and permit enhanced mechanical bioeffects with the given microbubble dose upon therapeutic excitations. There is also a strong benefit of image monitoring which in turn guides localized microbubble accumulation and release of the payload. In large blood vessels, potentially all of these will contribute to therapeutic regimes involving acoustic cavitation, such as sonothrombolysis and trans-membrane drug delivery for atherosclerosis [35]. In this paper, a method for controlled microbubble accumulation through combining acoustic trapping with plane wave imaging (PWI) is presented. The use of custom ultrasonic beams to image, translate and retain microbubbles against physiologically relevant flow rates was investigated with a linear array transducer.

II. ACOUSTIC MICROBUBBLE TRAPPING AND IMAGING

This section details the implementation of a composite ultrasound sequence that combines both trapping and PWI modalities. An acoustic trap field comprised of phase and amplitude modulated beams affects microbubble flow behavior to achieve localized accumulation and the instantaneous switch to imaging beams is expected to track microbubbles.

By considering a linear array transducer with N active elements that is split into two equal apertures, two equivalent but π phase-shifted plane waves were emitted simultaneously from these subapertures ($N/2$ elements) and destructively interfered at the center of the field. Fig. 1(a) shows a normalized 3-D peak negative pressure (PNP) field (an animation can be found in Supplementary Video S1 🖳) using the Field II package [36] with parameters given in Table I. To ensure clarity of the figure values below a threshold of −25 dB were removed. The arrow in Fig. 1(a) shows the flow direction of microbubbles. An acoustic null at the center of the acoustic field produces the pressure gradients required for the trapping effect to arrest microbubbles in flow. To visualize the null zone in the elevation direction, the −6-dB acoustic field at the depth of 35 mm is shown in Fig. 1(b). This plot was normalized by its own maximum value and the 35 mm depth was chosen to match the experimental setup in Section IV-B. The input beam [Fig. 1(c)] reduces the microbubble velocity through a primary radiation force that opposes the direction of flow. A disadvantage of using all (128) elements is that the radial radiation
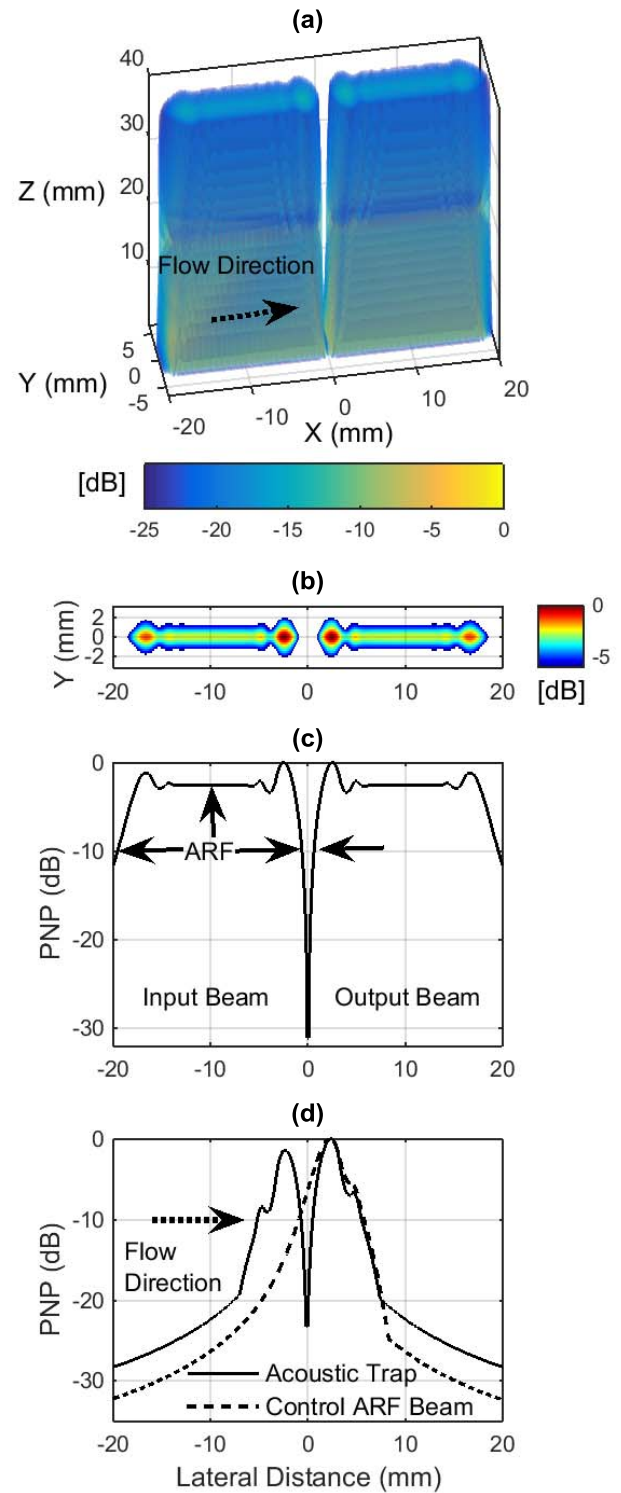

Fig. 1. PNP simulations by Field II. (a) Symmetric 3-D acoustic trap field. At the depth of 35 mm: (b) −6-dB 2-D acoustic field; PNP profiles by emitting π phase shifted (c) symmetric and (d) asymmetric plane wave beams. The number of active elements (N) that were excited for the acoustic trap was 128 for (a)–(c) and 64 for (d). The control ARF beam in (d) was emitted by the 32-element output aperture. For the acoustic trap and control ARF beam in Fig. 1(d), an asymmetric Hann apodization window was applied to the central 64 elements.

force within the inlet region impedes microbubbles entering the trapping region [Fig. 1(c)]. To address this, the pressure was lowered by asymmetrically apodizing the outer elements

| Parameter	Value
Number of elements	128
Pitch size	0.30 mm
Element height	6 mm
Elevation focus	20 mm
Center frequency	7.55 MHz
Bandwidth (-6 dB)	0.90 (fractional)
Sampling frequency	160 MHz
Excitation signal	3-cycle sinusoid (7 MHz)
Speed of sound	1547 m/s (Section IV-A)
Acoustic attenuation	0.42 dB·cm^{-1}·MHz^{-1} (Section IV-A)

Fig. 2. At the depth of 35 mm, (a) the simulated and modeled lateral pressure patterns at the moment $t = 0$ in (3), and (b) the lateral radiation force on a 2.2-μm microbubble based on parameters given in Table II.

of the array. Parameters relating to this operation were set for the given flow condition and more information about the ultrasound parameters is given in Section IV-B. The resulting simulation of the acoustic trap is shown in Fig. 1(d). The asymmetric trapping beam generates a lower pressure at the inlet, compared with that at the outlet. A single-peak ARF push beam resolved by emitting tapered plane waves only from the output aperture is also included in Fig. 1(d) as the control ARF beam in this study.

To monitor microbubble trapping, PWI pulses were interleaved with the trapping beams. Every full field-of-view 2-D image was acquired through a single plane wave transmission in PWI. It was adopted to preserve the trapping efficiency, by minimizing both the time needed for imaging and microbubble destruction [10], [11].

III. FORCES ON MICROBUBBLES IN A TRAPPING FIELD

In this section, the formulation of forces on a microbubble is undertaken followed by a simulation demonstrating the trapping effect on a single microbubble. The secondary radiation force that is produced by the microbubble rescattered field is neglected in the present method.

A. Primary Radiation Force

The use of a linear array simplifies analysis within the 2-D imaging plane. In a trapping field, microbubbles will experience the axial radiation force, as shown in [37], and a trapping force through the generation of lateral pressure gradients [38], [39]. Difficulties in characterizing the primary radiation force on microbubble populations, can arise from different configurations of the ultrasonic system, the microbubble size distribution and concentration as highlighted in [37]. But the force F on a single microbubble can be estimated by (1) [37], [40]

$$F = -\langle V(t)\nabla P \rangle \tag{1}$$

where $\langle \ \rangle$ indicates a time average, and $V(t)$ and ∇P are the microbubble volume and spatial pressure gradient, respectively.
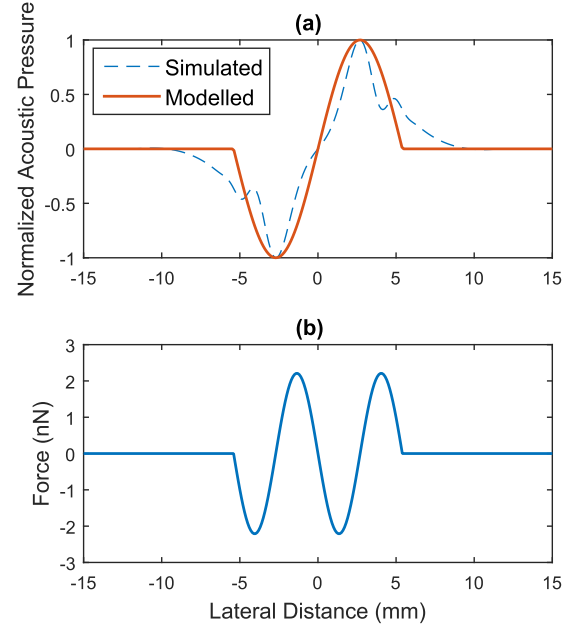
At a specific depth of the trapping field, the axial radiation force F_{axial} on a microbubble can be formulated by (2) [37]

$$F_{\text{axial}} = \frac{2\pi \, (P_a W_x)^2 \, D \, R_0}{\rho \, c \, \omega \, T} \frac{2\beta_{\text{tot}}/\omega}{[(\omega_0/\omega)^2 - 1)]^2 + (2\beta_{\text{tot}}/\omega)^2} \tag{2}$$

where P_a and W_x mean the peak acoustic pressure amplitude and the pressure amplitude modulation function in the direction (x) orthogonal to the incident field, respectively. D/T indicates the pulse duty cycle. ω and ω_0 denote the driving frequency and resonant frequency of the microbubble, respectively. R_0 is the equilibrium microbubble radius, ρ is the medium density, c is the speed of sound in the medium, and β_{tot} is the dimensionless damping coefficient.

In the direction perpendicular to the axial ultrasonic beam and at a specific depth, the amplitude modulated trapping field is modeled with a sinusoidal pattern [41]. The acoustic amplitude P_{lateral} along this direction which is defined by the axis x is thus written as follows:

$$P_{\text{lateral}} = P_0 + P_a B(x)\sin(kx)\cos(\omega t) \tag{3}$$

where P_0 is the constant hydrostatic pressure and t is time. $k = 2\pi/\lambda$ and $\lambda = 10.8$ mm is the wavelength of the modeled sinusoidal pattern which is given in Fig. 2(a). For simplicity, the symmetric trapping setup with 64 active elements transmitting 7-MHz traveling waves was configured for Fig. 2(a) and a Hann window was applied to the active aperture to modulate the pressure amplitude. The constant hydrostatic pressure is not shown in Fig. 2(a), and the simulated pressure profile was normalized by P_a as given in (2) and (3). $B(x)$ is a rectangular

window function, which is defined by

$$B(x) = \begin{cases} 1, & -\dfrac{\lambda}{2} < x < \dfrac{\lambda}{2} \\ 0, & \text{otherwise.} \end{cases} \tag{4}$$

The lateral pressure gradient $\nabla P_{\text{lateral}}$ is thus given by (5)

$$\nabla P_{\text{lateral}} = k P_{\text{a}} B(x) \cos(kx) \cos(\omega t). \tag{5}$$

Assuming linear amplitude oscillations, the microbubble volume can be modeled as (6) [40] for microbubbles with a resonant frequency below the ultrasound drive frequency

$$V(t) = V_0[1 - (3R_{e0}/R_0)\sin(kx)\cos(\omega t + \pi)] \tag{6}$$

where V_0 is the equilibrium microbubble volume and R_{e0} is the instantaneous variation of the microbubble radius, which is given by (7) [37]

$$R_{e0} = \frac{P_{\text{a}}}{R_0 \rho \omega^2 \sqrt{[(\omega_0/\omega)^2 - 1)]^2 + (2\beta_{\text{tot}}/\omega)^2}}. \tag{7}$$

Thus, the lateral radiation force F_{lateral} on a microbubble in a pulsed trapping field is deduced to be (8)

$$\begin{aligned} F_{\text{lateral}} &= -\left\langle V(t)\nabla P_{\text{lateral}}\frac{D}{T} \right\rangle \\ &= -\frac{3R_{e0}V_0\sin(2kx)kP_{\text{a}}B(x)}{4R_0}\frac{D}{T}. \end{aligned} \tag{8}$$

B. Stokes Drag Force and Microbubble Trapping

With the assumption that the microbubble radius does not change [37], [42], the Stokes drag force F_{drag} acting on one microbubble in fluid is given by (9) [37]

$$F_{\text{drag}} = 6\pi \eta R_0(v_{\text{f}} - v_{\text{b}}) \tag{9}$$

where η is the dynamic viscosity of the liquid and v_{b} and v_{f} are the microbubble and liquid velocity, respectively.

Considering a flow direction perpendicular to the axial ultrasonic beam, the lateral microbubble motion equation in a trapping field is given by (10), while neglecting the effect of gravity and buoyancy [41], [42]

$$m_{\text{b}}\frac{dv_{\text{b}}}{dt} + F_{\text{drag}} + F_{\text{lateral}} = 0 \tag{10}$$

where m_{b} is the microbubble mass.

A microbubble is trapped by the lateral radiation force, when $v_{\text{b}} = 0$ and $dv_{\text{b}}/dt = 0$ are satisfied in (9) and (10). In this case, the maximum speed $\|v_{\text{max}}\|$ of the microbubble which can be trapped is given by (11) through combining (8)–(10)

$$\|v_{\text{max}}\| = \left\| \frac{R_{e0}V_0\sin(2kx)kP_{\text{a}}B(x)}{8R_0{}^2\pi\eta}\frac{D}{T} \right\|. \tag{11}$$

A simulation was performed by assuming the presence of a 2.2-μm SonoVue microbubble in purified water, with the microbubble positioned at a depth of 35 mm relative to the transducer surface. The lateral radiation force on the microbubble is shown in Fig. 2(b) with parameters reported in Table II. Based on (11), the microbubble with a velocity up

TABLE II
PARAMETERS USED FOR FIG.2(B)

Parameter	Value
Trapping setup	Symmetric (see Fig.2a)
P_{a}	500 kPa
R_0	2.2 μm
ρ	998 kg/m^3
f	7 MHz
f_0	6.8 MHz [43]
$2\beta_{\text{tot}}/\omega$	$0.15\frac{f_0}{f}$ [37]
η	1 mPa.s
λ	10.8 mm (see Fig.2a)
$\frac{D}{T}$	50%

to 5.3 cm/s can be halted at the 1.4-mm position where the trapping force reaches its maximum assuming that the flow is entering from the left side.

The presence of the input beam would displace microbubbles to the side of a vessel as a result of the axial radiation force. The displacement could decrease the velocity of the microbubbles [27] before they enter the trap region, allowing a larger fraction of microbubbles arrested by the trapping force.

IV. EXPERIMENTAL TESTS

A tissue mimicking material (TMM) ultrasound flow phantom [44] was manufactured for the experimental component of this study. For all experimental conditions, both the trapping field and control ARF beam as described in Section II were used.

A. Ultrasound TMM Phantom Manufacture

A wall-less agar-based TMM flow phantom was made by mixing 36-g (3% by mass) agar power (Acros Organics, Geel, Belgium) and 25-g glass microspheres (P2011SL-2.5, Cospheric, Santa Barbara, USA) with filtered and degassed water. The mixture was then heated on a hot plate (Corning, Inc., Mexico) until the temperature reached 96 °C for 30 min. Glycerin (Value Health, Nottingham, U.K.) of 8% by mass and 10-g Germall plus (Gracefruit, Stirlingshire, U.K.) were added when the temperature was below 70 °C. The continuous stirring throughout the whole process permitted a uniform distribution of ultrasound scatters. Once mixed, the solution was poured into a container incorporated with a 2.8-mm plastic tube. The tube was removed after the phantom set to create a wall-less flow phantom. The average speed of sound and attenuation through this TMM was measured to be 1547 m/s and 0.42 dB·cm^{-1}·MHz^{-1}, respectively [45].

B. Flow Model and Experimental Parameters

The inlet of the 2.8-mm vessel at a depth of 35 mm (Fig. 3) was connected to a syringe, which was driven by a pump (Aladdin AL-1000, World Precision Instruments). The outlet was collected in a beaker and disposed of. At the ambient temperature 20 °C ±1 °C, SonoVue (Bracco S.p.A, Milan, Italy) solutions (diluted by 1:3000) were passed through the vessel with a constant flow rate of 56 mL/min ($V_{\text{mean}} = 152$ mm/s).

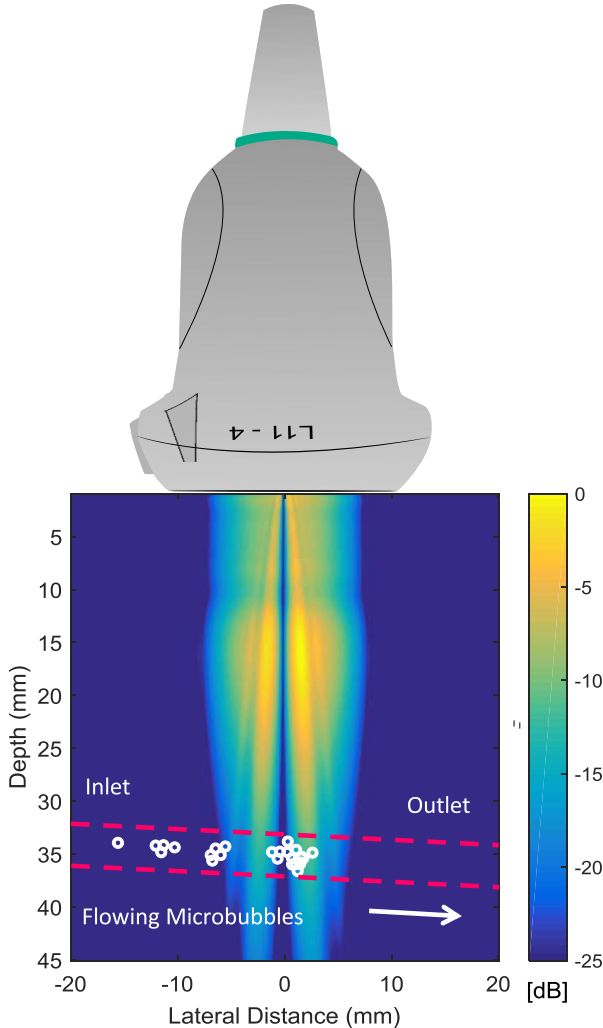| Flow model	Flow rate (mL/min)	Re	V_{max} (mm/s)	V_{mean} (mm/s)	Wall shear rate (s^{-1})	Flow condition
2.8-mm vessel	56	423	303	152	433	Laminar

Fig. 3. Schematic of the experimental setup with the simulated acoustic trap field (normalized PNP) superimposed onto the diagrammatic ultrasound flow phantom.
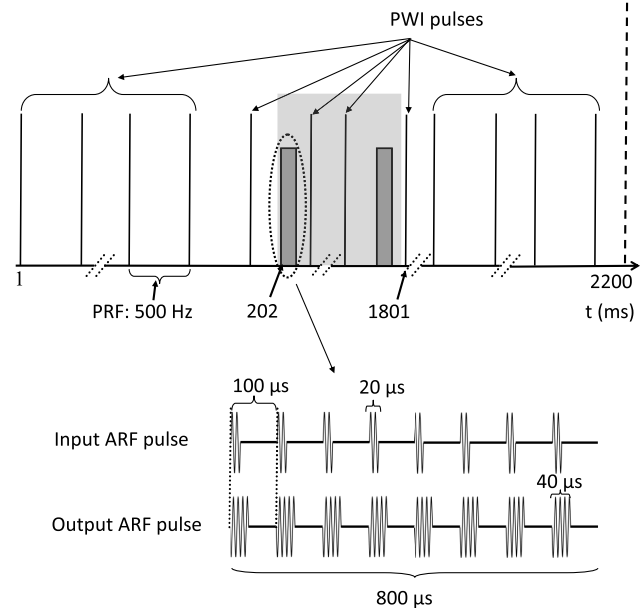

Fig. 4. Timing of emission sequences in experiments. ARF beams were interleaved with the imaging mode from 202 to 1801 ms and the shading shows one period. For clarity, ARF pulses emitted from two subapertures are diagramed.

Considering a Newtonian fluid, this flow corresponds to a shear rate of 433 s^{-1}, which is within the range of human arterial flow [46]. Inlet tubing of 50 cm ensured a constant parabolic flow profile within the imaging field as formulated by $L = 0.04 d Re$, where L is the entrance length for steady laminar flow, d is the diameter of the vessel, and Re is the Reynold's number [47]. The flow parameters are given in Table III.

The Ultrasound Array Research Platform II was programmed to generate the trapping and PWI modalities, in conjunction with a Verasonics L11-4 transducer (Verasonics, Inc., WA, USA). Each sequence consisted of dual excitations, the first being a long duration 7-MHz trapping waveform as

shown in Fig. 4, followed by a two-cycle 7.55-MHz PWI pulse. The transducer had a center frequency of 7.55 MHz with a −6-dB bandwidth of 90.8%.

A switching frequency of 1 kHz was chosen between two schemes, which resulted in a 500-Hz frame rate for imaging. Schematic illustrations of the sequence timing used in this study are shown in Fig. 4. The acoustic trap or control ARF beam was emitted in an intermittent way to protect the transducer (Fig. 4). ARF beams were activated between 202 and 1801 ms throughout the 2.2-s acquisition. For trapping microbubbles, the duty cycle ratio between the input and output apertures was empirically set to be 0.5 [38]. Only the output aperture was activated to emit the control ARF beam.

Pressures were measured through a 200-μm calibrated needle hydrophone (Precision Acoustics, Dorchester, U.K.) in water at the depth of 35 mm. The maximum PNP for ARF beams was estimated to be 320 kPa (mechanical index: 0.13 [48], [49]) after correcting for the attenuation of the phantom, and the mechanical index was tuned to 0.15 for imaging. For the given arterial flow condition, an aperture of 64 active elements was empirically set for the acoustic trap, and two 32-element subapertures were programmed to emit plane waves with the opposite phase polarity. The amplitude modulation of the beam as described in Section II was achieved through a pulse-width modulation scheme [50], [51]. At the depth of 35 mm, the measured PNP profile of the designed
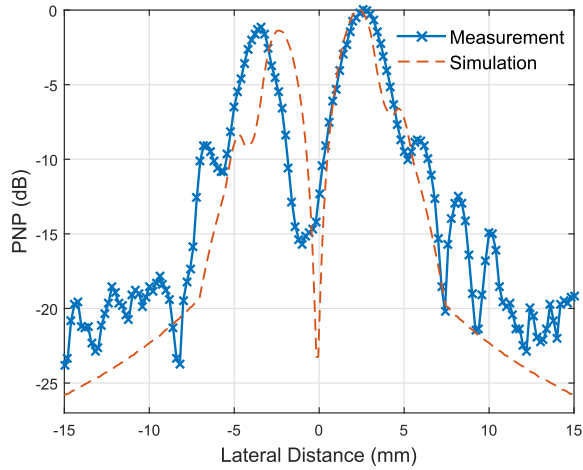
Fig. 5. Estimated and measured PNP profiles of the acoustic trap (center frequency: 7 MHz) at the depth of 35 mm. The maximum derated PNP = 320 kPa in the measurement.

TABLE IV

PARAMETERS IN BEAMFORMING AND THE SPECKLE TRACKING ALGORITHM

Parameter	Value
Axial beamforming step	9.7 μm
Lateral beamforming step	75.0 μm
Axial kernel size	0.621 mm
Lateral kernel size	1.800 mm
Lateral kernel overlapping	50%
Axial kernel overlapping	50% or 66%

acoustic trap is given in Fig. 5 and compared with its simulated counterpart. Meanwhile, the improvement of lateral resolution in PWI is expected due to a larger aperture when all 128 elements are used to create each line in the image. Thus, all 128 elements were active for PWI.

All the raw data were subsequently transferred and saved to a local drive for offline post processing with MATLAB (The MathWorks, Natick, MA, USA).

C. Analysis of Trapping Effects

The trapping force on the microbubble populations was used to affect their flow behavior and retard them. Vector flow mapping through a custom speckle tracking algorithm [52] was then used to provide a vector flow overlay to track microbubble trajectories, before, during, and after trapping. Briefly, RF frames were formed by using the delay and sum beamformation [8] with fixed axial and lateral sampling grids, followed by interframe displacement estimations. Displacements were first determined by a correlation-based pattern matching method in integer pixels. Accompanied by the median filtering and subpixel Gaussian interpolation [53], estimated displacements in conjunction with the known frame rate were used to render flow vectors within an ROI. Parameters in this processing are given in Table IV.

The influence, if any, of the vector density on the analysis of vector flow mapping was established by changing the

size of the overlapped regions between blocks for equivalent measurements. The axial and lateral kernel sizes are listed in Table IV [54]. This shows they were estimated with the ability to track the maximum velocity of 303 mm/s in this study (see Table III). In each test, the interrogation window size and the lateral kernel overlapping size were kept same, while the percentage of the axial window overlapping was varied between 50% and 66%.

A consequence of speed deceleration, caused by the trapping field, was that a greater quantity of microbubbles were deposited within the trap. The cumulative brightness (enveloped data) of microbubbles within ROIs was used to proportionally correlate microbubble quantities over time. The intensity baseline of this approach, was determined by replacing microbubble solutions with purified water.

For statistical analysis, a one-way ANOVA was used to demonstrate the statistical significance with a p value smaller than 0.05.

V. EXPERIMENTAL RESULTS

A. Effects of a Trapping Field on Microbubble Flow Dynamics

Fig. 6 shows the representative images acquired for, from top to bottom, water only, free-flowing microbubbles, microbubbles with the trapping field and microbubbles in combination with the control ARF beam. Schematic diagrams of PNP profiles across the vessel axis are added to Fig. 6(c) and (d).

In the presence of microbubbles, color coded vector maps were superimposed onto corresponding gray scale images reconstructed from single plane wave pulses. These gray scale images are shown with a dynamic range of 40 dB in Fig. 6. The orientation of each arrow indicates the averaged interframe microbubble trace within that kernel, whilst the arrow length correlates the speed. In velocity estimations, the interrogation window occupied a depth span of 0.621 mm and a lateral width of 1.800 mm (see Table IV). The axial kernel overlapping of 50% was used for still vector flow frames in Fig. 6. Two adjacent PWI RF frames were needed to resolve a single vector flow frame, and no multiframe averaging was applied to smooth the velocity profile.

Fig. 6(a) is a reference frame without microbubbles. The ROI within the flow channel showing microbubble trajectories was defined with dotted lines and utilized with all the data. The flow condition in this study was estimated to be steady (see Table III) and the resulting laminar flow would follow a parabolic pattern, with zero speed at the wall. With identical parameter sets used for Fig. 6(b)–(d), the noise floor of vector flow mapping was determined by processing one reference data set with purified water pumped through the channel at a rate of 56 mL/min (see Section IV-C). Consequently, 1100 PWI RF frames (or 1099 vector flow maps) were used and the noise floor was found to be 1.2 ± 0.6 mm/s (mean value $\pm$ 3 standard deviations). To improve clarity, a threshold of 5 mm/s which is above the noise floor was used for labeling flow vector estimations as green dots, indicative of the occurrence of trapped microbubbles. Other values above
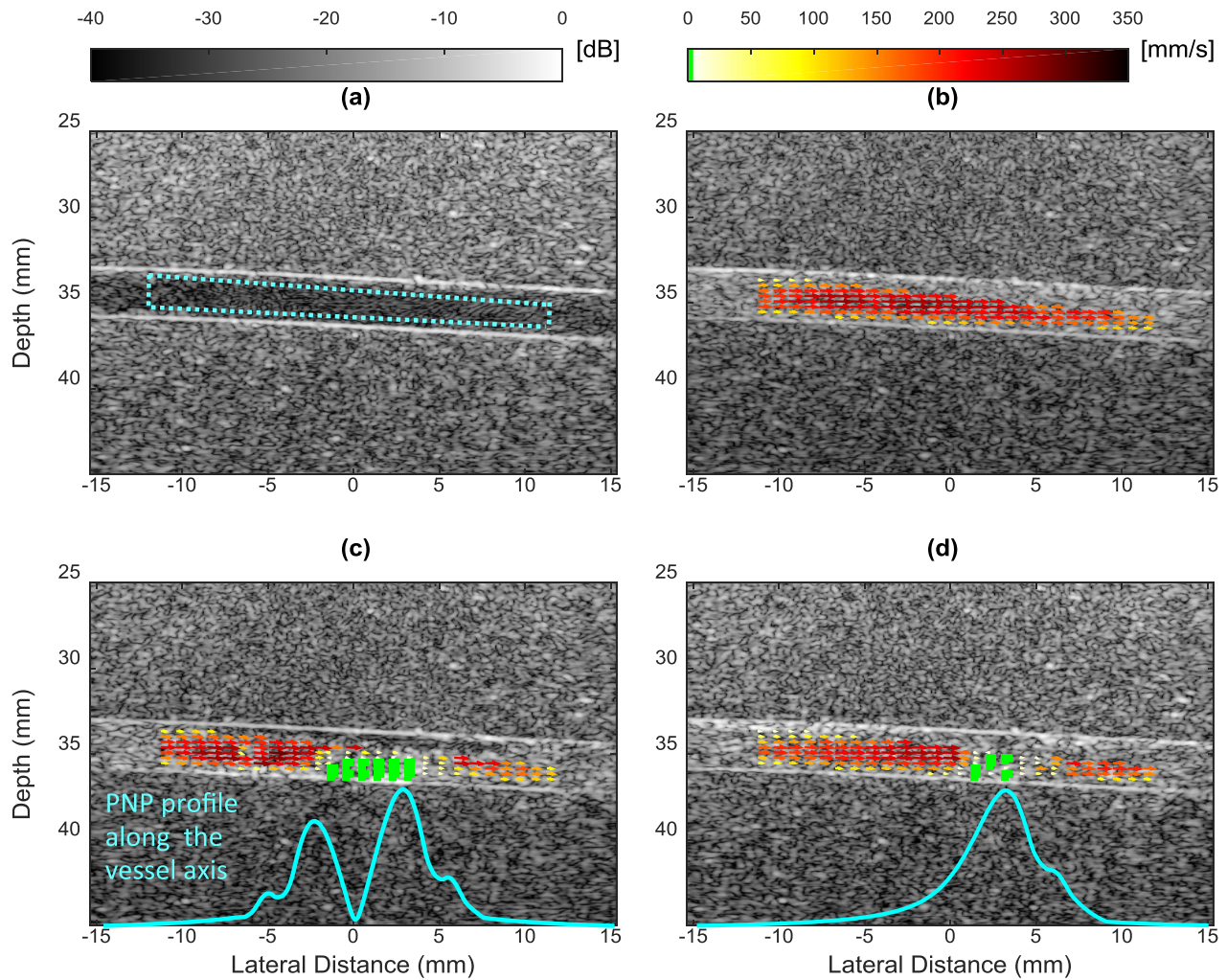
Fig. 6. Examples of captured frames for (a) water, (b) freely flowing microbubbles, (c) microbubbles with the acoustic trap, and (d) microbubbles with the control ARF beam. In the presence of microbubbles, composite images are shown with the vector flow overlay. Flow vectors with a velocity slower than 5 mm/s are highlighted with green dots.

the noise floor for velocity estimations could be used and the threshold of 5 mm/s was heuristically adopted for reporting. No flow direction information was available at these locations. The ROI was chosen to exclude flow vectors on the wall.

Supplementary Video S2 shows one example of the temporal evolution of microbubble flow patterns with acoustic trapping. To reject noise mainly residing in the deep location, the singular value decomposition (SVD) filter [55] was introduced when producing the video. Interleaving the acoustic trapping beam with PWI pulses resulted in nonuniform microbubble flow speeds in the inlet, trap, and outlet regions (Fig. 6). When the eigen-based SVD filter was first applied to the global plane wave data, the complex spatially varying microbubble speed affected the consequential microbubble speckle pattern and complicated the velocity estimation. The blockwise SVD filtering has been suggested [56] to tackle spatially varying characteristics but with heavy computational burdens. To simplify the processing in this study, the beamformed plane wave RF frames were divided into the contrast region and the tissue background, and only the
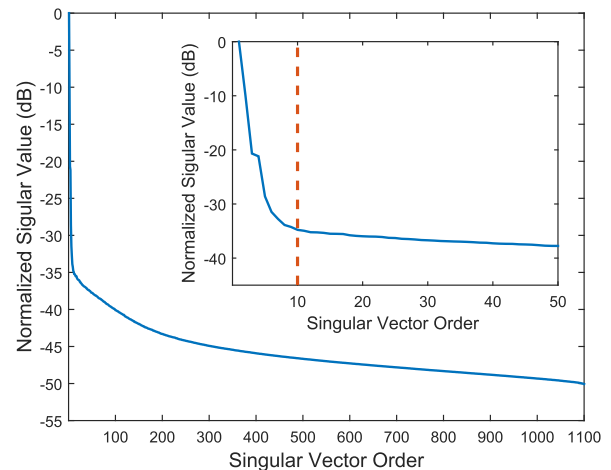

Fig. 7. Singular value distribution for the data used in Supplementary Video S2. Inset: expanded view of the singular value distribution with a separation line showing the cutoff order of 10.

tissue background was spatio-temporally processed to remove noise. Noise is supposed to be described by higher order
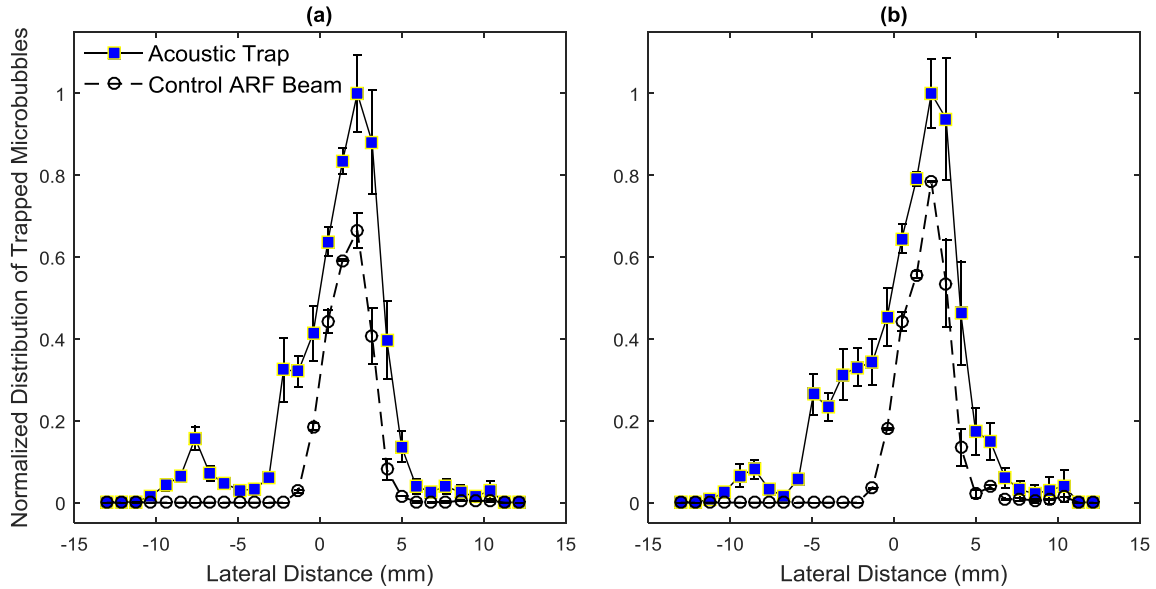
Fig. 8. Normalized distributions of trapped microbubbles along the lateral axis are shown by summing green dots from vector flow maps. The mean value and standard deviation are given from three repeated trials. (a) Axial kernel overlapping: 50%. (b) Axial kernel overlapping: 66%.

singular vectors which have smaller singular values [55]. The SVD filter order was chosen to be 10 from which the singular value curve starts to flatten [56] as shown in Fig. 7. Flow dynamics were tracked with the method detailed earlier. The axial kernel overlapping of 50% was employed in velocity estimations and the video was played back at 25 fps.

To show the effect of the acoustic trap and control ARF beam on the flow profile, first a control experiment without any ARF beams was performed to calculate the baseline [Fig. 6(b)]. Before the activation of ARF beams at $t = 202$ ms, there are no visible green dots representing trapped microbubbles. Fig. 6(c) shows a single snapshot of microbubble flow dynamics when the acoustic trap is active. Although the microbubble flow changes with time (see Supplementary Video S2🖥), the speed of microbubbles reduces significantly within the trapping region, with green dots showing trapped microbubbles. When compared with results by using the control ARF beam in Fig. 6(d), the acoustic trap in Fig. 6(c) enables more microbubble accumulation also in the lumen. Once acoustic trapping beams ceased at $t = 1801$ ms, the microbubble trajectories follow a laminar flow pattern similar to Fig. 6(b), as shown in Supplementary Video S2🖥.

The two different axial kernel overlapping sizes in Table IV were used to manipulate the density of flow vectors within the unaltered ROI. In each trail, the number of green labels was counted with the vector flow frame 101 to 900, considering the period (from 202 to 1801 ms) with the application of ARF beams. Normalized values are portrayed spreading the lateral axis as shown in Fig. 8. With the identical setup in velocity mapping, in comparison to experiments with the control ARF beam, where the drag force overcomes the counterflow radiation force, the acoustic trap shows the enhanced capability of microbubble accumulation ($p < 0.05$) for both the conditions in Fig. 8.

B. Effects of a Trapping Field on Microbubble Signal Amplitude Curves

Three ROIs were defined and allocated at the inlet, the designed trapping region and the outlet as shown in Fig. 9(a). Signal magnitude curves are presented as a function of time over three repeated trials in Fig. 9(b)–(d).

During the first 202 ms duration without the use of ARF, no significant magnitude differences were observed [Fig. 9(c) and (d)]. In the following 1.6-s period with the application of the acoustic trap, signal amplitudes from all three ROIs showed increases until approaching a steady state, whereas in control experiments, the similar increasing trend of intensities occurred only in the trap and outlet ROIs. During the last 200 ms, specific to the trap ROI, an instantaneous signal increase was perceptibly observable after the cessation of ARF [Fig. 9(c) and (d)]. However, much higher amplitudes were obtained with the acoustic trap. A secondary radiation force that was generated from microbubble rescattered fields, can be attractive or repulsive determined by the relationship of microbubble vibration phases. In response to ARF beams, the secondary radiation force was present as aggregating microbubbles during sonication. The dispersion of microbubble clusters after ceasing ARF has been demonstrated to be responsible for the transient amplitude enhancement [29], [57]. Thus, the prediction of microbubble quantities through image intensities would only be reliable after deactivating ARF beams. Consequently, within the trap ROI from 1900 to 2200 ms, the acoustic trap led to an average amplitude improvement of 71% $\pm$ 28% ($n = 3$, $p < 0.05$) over the control, indicating more efficient microbubble localization.

VI. DISCUSSION

With a linear array transducer, this paper demonstrated the use of acoustic trapping and PWI to facilitate localized microbubble accumulation. The proposed scheme was
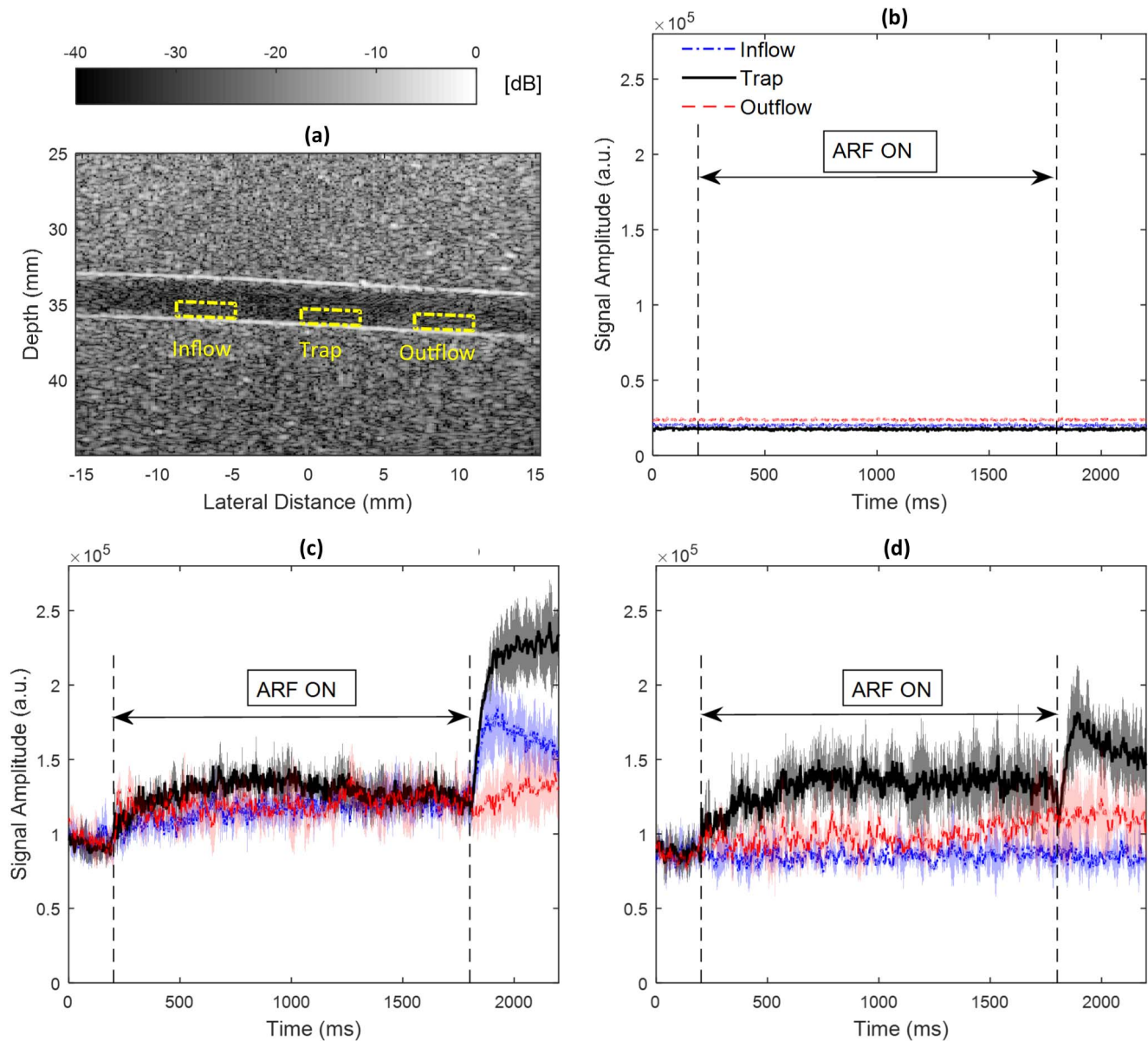
Fig. 9. Average intensity curves in (a) ROIs are displayed as a function of time, for (b) water, (c) microbubbles + the acoustic trap, and (d) microbubbles + the control ARF beam. Results are shown with the mean and standard deviation from three trials.

illustrated by simulating and measuring the beam pattern and further verified with a wall-less flow phantom. Greater microbubble accumulation was achieved within an ROI in a controlled way when the trapping field was activated. The interleaved PWI modality enabled the monitoring of this process. In the presence of additional therapeutic excitations, accumulated bare microbubbles using the proposed scheme are expected to enhance microbubble-cell interactions resultant from the increased microbubble concentration [32]. When microbubbles are functionalized or attached with a therapeutic payload such as a liposome [58], a localized payload release, and possibly control of the concentration of payload through varying the cluster size, could be achieved by using a single transducer performing microbubble trapping, imaging, and destruction.

Influenced by the ARF beams, the secondary radiation force from the microbubble rescattered pressure field aggregates microbubbles. The microbubble cluster dynamics could be described with an identical model for a single microbubble through inputting the cluster radius to the system [17]. Consequently, clusters will resonate at a lower driving frequency. It is difficult to estimate the cluster radii *in vivo* making the resonant frequency unpredictable, which could affect imaging or payload release. When microbubbles are clustered, it is hard to destroy them. However, after the trap is ceased they start to disperse. The instant increase of microbubble intensities in Fig. 9(c) and (d) is illustrated as a result of microbubble cluster dispersion [29], [57]. Thus, it would be possible to destroy them and maximize release from a therapeutic microbubble by setting an appropriate

time delay between the destruction pulse and trapping beam.

Quantifying trapped microbubbles with ultrasound imaging is challenging. The off-resonance driving, attenuation, and acoustic shadowing are responsible for the suppression of the intensity increase, irrelative with the real microbubble concentration. The size of clusters or the number of microbubbles cannot be estimated from the B-mode or contrast mode images when the trapping beam is active. In this study, the image brightness after deactivating ARF beams, as shown in Fig. 9 (c) and (d) between 1900 and 2200 ms, was quantified and the acoustic trap showed an average gain of $71\% \pm 28\%$ ($n = 3$, $p < 0.05$) relative to the control ARF beam.

The use of the 1-D linear array lacks the capability of beamforming along the elevation axis, which limits acoustic trapping as one in-plane method. Given the 3-D nature of vascular anatomy and blood flow, a 2-D array would be of immense importance which enables simultaneous microbubble trapping and imaging in a 3-D volume. With a fully addressed 2-D array, the high channel count would place a heavy burden on electronics. The optimized sparse array could be a good candidate, which maintains moderate acoustic field patterns but with much reduced active elements [59]. Although having a limitation in the elevation direction, the experimental comparison between the acoustic trap and a control ARF beam showed that the acoustic trap retained a larger microbubble population in the lumen area of a 2.8-mm vessel (Fig. 6c). This would be advantageous in cases where targets are not only located along the distal wall. Potentially, benefiting from the two-peak acoustic trap and the counterflow radiation force, microbubble localization would be more resistant to the pulsatile nature of blood flow.

Narrower acoustic trapping regions can be achieved with higher driving frequencies resulting from shorter wavelengths. But the use of higher frequencies will be prone to higher attenuation. A center frequency of 7 MHz was used for trapping in this study, but the easy control of electronics enables the flexible frequency modification for vessels at different depths.

PWI should be operated in a real-time and continuous manner to assist motion detection, which is very important to keep the trap always in the targeted region. The use of a graphics processing unit-based beamformer [60] may allow for the fast realization of PWI. To selectively image microbubbles, nonlinear imaging modalities such as subharmonic imaging [44], [61], pulse inversion, or amplitude modulation [62] can be further investigated.

There are multiple ways to manipulate the formation of the acoustic trap to accommodate different flow rates. For example, adjusting the driving voltage or dynamically apodizing the aperture of the transducer, could account for variable pressure slopes in the trap field, and thus simple ways to engender varying counterflow radiation forces. For the given flow condition in this study, empirically determined parameters were used for trapping microbubbles. More automated approaches to determine the required acoustical parameters should be further investigated. The fast realization of PWI could also

make it possible to have the necessary feedback loop and guide the determination of required parameters.

The use of purified water as circulating fluid in a wall-less flow phantom is a simplified experimental demonstration of a complex *in vivo* application. The presence of other molecules within the blood stream, red blood cells, for example, could interfere with microbubble trapping. The relative angle between the transducer and the vessel would affect the performance of the proposed method, which could be optimized through imaging prior to trapping. As the angle increases, so does the trapping efficiency. To make this scheme more widely adopted, a solution that could be employed is to tilt the transducer or electronically steer the beam, as is broadly used in ultrasonic color Doppler imaging.

VII. CONCLUSION

The capability of localized accumulation of microbubbles holds promise for the enhanced therapeutic use of microbubbles to treat vascular diseases. In this paper, one scheme allowing for simultaneous microbubble trapping and imaging was proposed and demonstrated. After a period of 1.6 s with ARF beams interleaved, the acoustic trap outperformed the control, with slower microbubble speeds in the center of the sound field ($p < 0.05$) and an enhancement of $71\% \pm 28\%$ ($p < 0.05$) in image brightness. The easy control of electronics would enable this scheme applicable to a range of flow conditions, and with attachment of drugs to microbubbles, further amplified merits would be anticipated.

REFERENCES

[1] R. Senior *et al.*, "Contrast echocardiography: Evidence-based recommendations by European association of echocardiography," *Eur. J. Echocardiogr.*, vol. 10, no. 2, pp. 194–212, 2009.
[2] V. Battaglia and R. Cervelli, "Liver investigations: Updating on US technique and contrast-enhanced ultrasound (CEUS)," *Eur. J. Radiol.*, vol. 96, pp. 65–73, Nov. 2017.
[3] T. Faez, M. Emmer, K. Kooiman, M. Versluis, A. F. W. van der Steen, and N. de Jong, "20 years of ultrasound contrast agent modeling," *IEEE Trans. Ultrason., Ferroelect., Freq. Control*, vol. 60, no. 1, pp. 7–20, Jan. 2013.
[4] T. G. Leighton, "What is ultrasound?" *Prog. Biophys. Mol. Biol.*, vol. 93, nos. 1–3, pp. 3–83, Jan./Apr. 2007.
[5] P. Phillips and E. Gardner, "Contrast–agent detection and quantification," *Eur. Radiol. Supplements*, vol. 14, pp. P4–P10, Oct. 2004.
[6] F. Forsberg, W. T. Shi, and B. Goldberg, "Subharmonic imaging of contrast agents," *Ultrasonics*, vol. 38, nos. 1–8, pp. 93–98, 2000.
[7] A. Bouakaz, B. J. Krenning, W. B. Vletter, F. J. ten Cate, and N. de Jong, "Contrast superharmonic imaging: A feasibility study," *Ultrasound Med. Biol.*, vol. 29, no. 4, pp. 547–553, Apr. 2003.
[8] G. Montaldo, M. Tanter, J. Bercoff, N. Benech, and M. Fink, "Coherent plane-wave compounding for very high frame rate ultrasonography and transient elastography," *IEEE Trans. Ultrason., Ferroelect., Freq. Control*, vol. 56, no. 3, pp. 489–506, Mar. 2009.
[9] C. Papadacci, M. Pernot, M. Couade, M. Fink, and M. Tanter, "High-contrast ultrafast imaging of the heart," *IEEE Trans. Ultrason., Ferroelect., Freq. Control*, vol. 61, no. 2, pp. 288–301, Feb. 2014.
[10] O. Couture, M. Fink, and M. Tanter, "Ultrasound contrast plane wave imaging," *IEEE Trans. Ultrason., Ferroelect., Freq. Control*, vol. 59, no. 12, pp. 2676–2683, Dec. 2012.
[11] J. Viti, H. J. Vos, N. de Jong, F. Guidi, and P. Tortoli, "Detection of contrast agents: Plane wave versus focused transmission," *IEEE Trans. Ultrason., Ferroelect., Freq. Control*, vol. 63, no. 2, pp. 203–211, Feb. 2016.
[12] M. E. Toulemonde *et al.*, "High frame-rate contrast echocardiography: In-human demonstration," *JACC, Cardiovascular Imag.*, 2017, doi: 10.1016/j.jcmg.2017.09.011.

[13] C. Tremblay-Darveau, R. Williams, L. Milot, M. Bruce, and P. N. Burns, "Combined perfusion and Doppler imaging using plane-wave nonlinear detection and microbubble contrast agents," *IEEE Trans. Ultrason., Ferroelect., Freq. Control*, vol. 61, no. 12, pp. 1988–2000, Dec. 2014.

[14] C. Errico *et al.*, "Ultrafast ultrasound localization microscopy for deep super-resolution vascular imaging," *Nature*, vol. 527, no. 7579, pp. 499–502, Nov. 2015.

[15] M. de Saint Victor, C. Crake, C.-C. Coussios, and E. Stride, "Properties, characteristics and applications of microbubbles for sonothrombolysis," *Expert Opinion Drug Del.*, vol. 11, no. 2, pp. 187–209, 2014.

[16] K. Tachibana and S. Tachibana, "Albumin microbubble echo-contrast material as an enhancer for ultrasound accelerated thrombolysis," *Circulation*, vol. 92, no. 5, pp. 1148–1150, 1995.

[17] K. Kooiman, H. J. Vos, M. Versluis, and N. de Jong, "Acoustic behavior of microbubbles and implications for drug delivery," *Adv. Drug Delivery Rev.*, vol. 72, pp. 28–48, Jun. 2014.

[18] A. van Wamel *et al.*, "Vibrating microbubbles poking individual cells: Drug transfer into cells via sonoporation," *J. Controlled Release*, vol. 112, no. 2, pp. 149–155, May 2006.

[19] J. McLaughlan *et al.*, "Increasing the sonoporation efficiency of targeted polydisperse microbubble populations using chirp excitation," *IEEE Trans. Ultrason., Ferroelect., Freq. Control*, vol. 60, no. 12, pp. 2511–2520, Dec. 2013.

[20] J.-M. Escoffre *et al.*, "Doxorubicin liposome-loaded microbubbles for contrast imaging and ultrasound-triggered drug delivery," *IEEE Trans. Ultrason., Ferroelect., Freq. Control*, vol. 60, no. 1, pp. 78–87, Jan. 2013.

[21] I. Lentacker, S. C. De Smedt, and N. N. Sanders, "Drug loaded microbubble design for ultrasound triggered delivery," *Soft Matter*, vol. 5, no. 11, pp. 2161–2170, 2009.

[22] B. Petit *et al.*, "Sonothrombolysis: The contribution of stable and inertial cavitation to clot lysis," *Ultrasound Med. Biol.*, vol. 41, no. 5, pp. 1402–1410, 2015.

[23] M. Ward, J. Wu, and J.-F. Chiu, "Experimental study of the effects of optison concentration on sonoporation in vitro," *Ultrasound Med. Biol.*, vol. 26, no. 7, pp. 1169–1175, 2000.

[24] Y. Liu, H. Miyoshi, and M. Nakamura, "Encapsulated ultrasound microbubbles: Therapeutic application in drug/gene delivery," *J. Controlled Release*, vol. 114, no. 1, pp. 89–99, 2006.

[25] K. Ferrara, R. Pollard, and M. Borden, "Ultrasound microbubble contrast agents: Fundamentals and application to gene and drug delivery," *Annu. Rev. Biomed. Eng.*, vol. 9, pp. 415–447, Aug. 2007.

[26] A. M. Takalkar, A. L. Klibanov, J. J. Rychak, J. R. Lindner, and K. Ley, "Binding and detachment dynamics of microbubbles targeted to P-selectin under controlled shear flow," *J. Controlled Release*, vol. 96, no. 3, pp. 473–482, 2004.

[27] P. Dayton, A. Klibanov, G. Brandenburger, and K. Ferrara, "Acoustic radiation force in vivo: A mechanism to assist targeting of microbubbles," *Ultrasound Med. Biol.*, vol. 25, no. 8, pp. 1195–1201, 1999.

[28] R. C. Gessner, J. E. Streeter, R. Kothadia, S. Feingold, and P. A. Dayton, "An in vivo validation of the application of acoustic radiation force to enhance the diagnostic utility of molecular imaging using 3-D ultrasound," *Ultrasound Med. Biol.*, vol. 38, no. 4, pp. 651–660, 2012.

[29] S. Wang, J. A. Hossack, A. L. Klibanov, and F. W. Mauldin, Jr., "Binding dynamics of targeted microbubbles in response to modulated acoustic radiation force," *Phys. Med. Biol.*, vol. 59, no. 2, pp. 465–484, 2013.

[30] A. V. Patil, J. J. Rychak, A. L. Klibanov, and J. A. Hossack, "Real-time technique for improving molecular imaging and guiding drug delivery in large blood vessels: *In vitro* and *ex vivo* results," *Mol. Imag.*, vol. 10, no. 4, pp. 7290–2011, 2011.

[31] J. Owen, Q. Pankhurst, and E. Stride, "Magnetic targeting and ultrasound mediated drug delivery: Benefits, limitations and combination," *Int. J. Hyperthermia*, vol. 28, no. 4, pp. 362–373, 2012.

[32] C. Crake *et al.*, "Passive acoustic mapping of magnetic microbubbles for cavitation enhancement and localization," *Phys. Med. Biol.*, vol. 60, no. 2, pp. 785–806, 2015.

[33] C. Crake *et al.*, "Enhancement and passive acoustic mapping of cavitation from fluorescently tagged magnetic resonance-visible magnetic microbubbles in vivo," *Ultrasound Med. Biol.*, vol. 42, no. 12, pp. 3022–3036, 2016.

[34] L. C. Barnsley, D. Carugo, and E. Stride, "Optimized shapes of magnetic arrays for drug targeting applications," *J. Phys. D, Appl. Phys.*, vol. 49, no. 22, p. 225501, 2016.

[35] F. E. Shamout *et al.*, "Enhancement of non-invasive trans-membrane drug delivery using ultrasound and microbubbles during physiologically relevant flow," *Ultrasound Med. Biol.*, vol. 41, no. 9, pp. 2435–2448, Sep. 2015.

[36] J. A. Jensen and N. B. Svendsen, "Calculation of pressure fields from arbitrarily shaped, apodized, and excited ultrasound transducers," *IEEE Trans. Ultrason., Ferroelect., Freq. Control*, vol. 39, no. 2, pp. 262–267, Mar. 1992.

[37] P. A. Dayton, K. E. Morgan, A. L. Klibanov, G. Brandenburger, K. R. Nightingale, and K. W. Ferrara, "A preliminary evaluation of the effects of primary and secondary radiation forces on acoustic contrast agents," *IEEE Trans. Ultrason., Ferroelect., Freq. Control*, vol. 44, no. 6, pp. 1264–1277, Jun. 1997.

[38] S. Harput *et al.*, "Simultaneous trapping and imaging of microbubbles at clinically relevant flow rates," in *Proc. IEEE Int. Ultrason. Symp. (IUS)*, Sep. 2016, pp. 1–4.

[39] B. Raiton, J. R. McLaughlan, S. Harput, P. R. Smith, D. M. J. Cowell, and S. Freear, "The capture of flowing microbubbles with an ultrasonic tap using acoustic radiation force," *Appl. Phys. Lett.*, vol. 101, no. 4, p. 044102, 2012.

[40] T. G. Leighton, A. J. Walton, and M. J. W. Pickworth, "Primary Bjerknes forces," *Eur. J. Phys.*, vol. 11, no. 1, p. 47, 1990.

[41] Y. Yamakoshi and Y. Noguchi, "Micro particle trapping by opposite phases ultrasonic travelling waves," *Ultrasonics*, vol. 36, no. 8, pp. 873–878, 1998.

[42] P. Tortoli, M. Pratesi, and V. Michelassi, "Doppler spectra from contrast agents crossing an ultrasound field," *IEEE Trans. Ultrason., Ferroelect., Freq. Control*, vol. 47, no. 3, pp. 716–726, May 2000.

[43] J.-M. Gorce, M. Arditi, and M. Schneider, "Influence of bubble size distribution on the echogenicity of ultrasound contrast agents: A study of SonoVue," *Investigative Radiol.*, vol. 35, no. 11, pp. 661–671, 2000.

[44] S. Harput, M. Arif, J. McLaughlan, D. M. J. Cowell, and S. Freear, "The effect of amplitude modulation on subharmonic imaging with chirp excitation," *IEEE Trans. Ultrason., Ferroelect., Freq. Control*, vol. 60, no. 12, pp. 2532–2544, Dec. 2013.

[45] J. E. Browne, K. V. Ramnarine, A. J. Watson, and P. R. Hoskins, "Assessment of the acoustic properties of common tissue-mimicking test phantoms," *Ultrasound Med. Biol.*, vol. 29, no. 7, pp. 1053–1060, Jul. 2003.

[46] S.-K. Jeong and R. S. Rosenson, "Shear rate specific blood viscosity and shear stress of carotid artery duplex ultrasonography in patients with lacunar infarction," *BMC Neurol.*, vol. 13, no. 1, p. 36, 2013.

[47] C. H. Leow, E. Bazigou, R. J. Eckersley, A. C. Yu, P. D. Weinberg, and M.-X. Tang, "Flow velocity mapping using contrast enhanced high-frame-rate plane wave ultrasound and image tracking: Methods and initial in vitro and in vivo evaluation," *Ultrasound Med. Biol.*, vol. 41, no. 11, pp. 2913–2925, 2015.

[48] R. E. Apfel and C. K. Holland, "Gauging the likelihood of cavitation from short-pulse, low-duty cycle diagnostic ultrasound," *Ultrasound Med. Biol.*, vol. 17, no. 2, pp. 179–185, Jan. 1991.

[49] C. C. Church, "Frequency, pulse length, and the mechanical index," *Acoust. Res. Lett. Online*, vol. 6, no. 3, pp. 162–168, 2005.

[50] P. R. Smith, D. M. J. Cowell, and S. Freear, "Width-modulated square-wave pulses for ultrasound applications," *IEEE Trans. Ultrason., Ferroelect., Freq. Control*, vol. 60, no. 11, pp. 2244–2256, Nov. 2013.

[51] D. Cowell and S. Freear, "Quinary excitation method for pulse compression ultrasound measurements," *Ultrasonics*, vol. 48, no. 2, pp. 98–108, 2008.

[52] L. Nie, S. Harput, D. M. J. Cowell, and S. Freear, "Velocity estimation error reduction in stenosis areas using a correlation correction method," in *Proc. IEEE Int. Ultrason. Symp. (IUS)*, Sep. 2016, pp. 1–4.

[53] L. Niu *et al.*, "Ultrasonic particle image velocimetry for improved flow gradient imaging: Algorithms, methodology and validation," *Phys. Med. Biol.*, vol. 55, no. 7, p. 2103, 2010.

[54] M. Lenge, A. Ramalli, E. Boni, H. Liebgott, C. Cachard, and P. Tortoli, "High-frame-rate 2-D vector blood flow imaging in the frequency domain," *IEEE Trans. Ultrason., Ferroelect., Freq. Control*, vol. 61, no. 9, pp. 1504–1514, Sep. 2014.

[55] C. Demené *et al.*, "Spatiotemporal clutter filtering of ultrafast ultrasound data highly increases Doppler and fultrasound sensitivity," *IEEE Trans. Med. Imag.*, vol. 34, no. 11, pp. 2271–2285, Nov. 2015.

[56] P. Song, A. Manduca, J. D. Trzasko, and S. Chen, "Ultrasound small vessel imaging with block-wise adaptive local clutter filtering," *IEEE Trans. Med. Imag.*, vol. 36, no. 1, pp. 251–262, Jan. 2017.

[57] S. Wang, C. Y. Wang, S. Unnikrishnan, A. L. Klibanov, J. A. Hossack, and F. W. Mauldin, Jr., "Optical verification of microbubble response to acoustic radiation force in large vessels with in vivo results," *Investigative Radiol.*, vol. 50, no. 11, pp. 772–784, 2015.

[58] S. A. Peyman *et al.*, "Expanding 3D geometry for enhanced on-chip microbubble production and single step formation of liposome modified microbubbles," *Lab Chip*, vol. 12, no. 21, pp. 4544–4552, 2012.

[59] E. Roux, A. Ramalli, H. Liebgott, C. Cachard, M. C. Robini, and P. Tortoli, "Wideband 2-D array design optimization with fabrication constraints for 3-D US imaging," *IEEE Trans. Ultrason., Ferroelect., Freq. Control*, vol. 64, no. 1, pp. 108–125, Jan. 2017.

[60] B. Y. S. Yiu, I. K. H. Tsang, and A. C. H. Yu, "GPU-based beamformer: Fast realization of plane wave compounding and synthetic aperture imaging," *IEEE Trans. Ultrason., Ferroelect., Freq. Control*, vol. 58, no. 8, pp. 1698–1705, Aug. 2011.

[61] J. R. McLaughlan, S. Harput, R. H. Abou-Saleh, S. A. Peyman, S. Evans, and S. Freear, "Characterisation of liposome-loaded microbubble populations for subharmonic imaging," *Ultrasound Med. Biol.*, vol. 43, no. 1, pp. 346–356, 2017.

[62] R. J. Eckersley, C. T. Chin, and P. N. Burns, "Optimising phase and amplitude modulation schemes for imaging microbubble contrast agents at low acoustic power," *Ultrasound Med. Biol.*, vol. 31, no. 2, pp. 213–219, Feb. 2005.

Thomas M. Carpenter received the M.Eng. degree in electronic and electrical engineering from the University of Leeds, Leeds, U.K., in 2014. He is currently pursuing the Ph.D. degree with the Ultrasound Group, University of Leeds.

He joined Georgia Institute of Technology, Atlanta, GA, USA, as a Research Engineer, developing high-speed FPGA designs for ultrasound imaging applications. He is currently a Research Assistant with the Ultrasound Group, University of Leeds. His main research focus is embedded systems and FPGA design, both in the biomedical field and for industrial applications.

Luzhen Nie (S'16) received the M.Eng. degree in electronic and electrical engineering from the Harbin Institute of Technology, Harbin, China, in 2015. He is currently pursuing the Ph.D. degree with the Ultrasonics and Instrumentation Group, University of Leeds, Leeds, U.K.

His current research interests involve high frame-rate ultrasound imaging, microbubble contrast agents, Doppler and vector flow mapping.

James R. McLaughlan received the Ph.D. degree from the Institute of Cancer Research, London, U.K., with a focus on the optimization of therapeutic ultrasound for cancer therapy using cavitation.

In 2010, he joined the University of Leeds to work on next generation therapeutic microbubbles. He currently holds a joint academic position between the faculties of Engineering and Medicine and Health, where his main research areas are noninvasive cancer therapies, molecular-targeted theranostics and semi-autonomous surgical systems.

Dr. McLaughlan was a recipient of a Leverhulme Early Career Research Fellowship to develop molecular-targeted gold nanoparticles for the detection and treatment of cancerous cells in 2013.

Sevan Harput received the B.Sc. degree in microelectronics engineering and the M.Sc. degree in electronic engineering and computer sciences from Sabanci University, Istanbul, Turkey, in 2005 and 2007, respectively, and the Ph.D. degree from the University of Leeds, Leeds, U.K., in 2013.

He is currently a Research Associate with the Department of Bioengineering, Imperial College London, London, U.K., and a Visiting Scholar with King's College London, London, and the University of Leeds. He has been an Editorial and Administrative Assistant in the IEEE TRANSACTIONS ON ULTRASONICS, FERROELECTRICS, AND FREQUENCY CONTROL since 2013. His research interests focus on high frame-rate ultrasound imaging, super-resolution imaging, ultrasound contrast agents, signal processing for biomedical imaging, nonlinear acoustics, ultrasound sensor modeling, and biomedical device development.

Steven Freear (S'95–M'97–SM'11) received the Ph.D. degree from the University of Leeds, Leeds, U.K., in 1997.

He worked in the electronics industry for 7 years as a medical ultrasonic system designer. He was appointed Lecturer (Assistant Professor), Senior Lecturer (Associate Professor), and then Professor with the School of Electronic and Electrical Engineering, University of Leeds, in 2006, 2008, and 2016, respectively. In 2006, he formed the Ultrasound Group, specializing in both industrial and biomedical research. In 2014, he was appointed Visiting Professor with the Georgia Institute of Technology, Atlanta, GA, USA. He is an External Examiner to undergraduate programs in Electronic Engineering at Queen's University, Belfast, U.K. His main research interest is concerned with advanced analog and digital signal processing and instrumentation for ultrasonic systems. He teaches digital signal processing, VLSI and embedded systems design, and hardware description languages at both undergraduate and postgraduate levels.

Dr. Freear was elected Editor-in-Chief in 2013 for the IEEE TRANSACTIONS ON ULTRASONICS, FERRORELECTRICS, AND FREQUENCY CONTROL.

David M. J. Cowell received the Ph.D. degree from the University of Leeds, Leeds, U.K., in 2008, with a focus on advanced coding techniques and excitation circuit design for industrial instrumentation and medical imaging ultrasound systems.

He performed extensive consultancy in instrumentation, field-programmable gate arrays, and high-speed digital hardware design. Following work as a research consultant in measurement and instrumentation, he joined the Ultrasound Group, University of Leeds, as a Research Fellow, where his research is currently focused on noninvasive industrial ultrasound measurement and advanced miniaturized ultrasound excitation systems with low harmonic distortion for phased array imaging, ultrasound system design, and signal processing.